

# ***IMAGING-BASED PATIENT-SPECIFIC BIOMECHANICAL EVALUATION OF ATHEROSCLEROSIS AND ANEURYSM: A COMPARISON BETWEEN STRUCTURAL-ONLY, FLUID-ONLY AND FLUID-STRUCTURE INTERACTION ANALYSIS***

Jessica Benitez Mendieta <sup>1,2</sup>, Phani Kumari Paritala <sup>1,2</sup>, Jiaqiu Wang <sup>1,2</sup>, Zhiyong Li <sup>1,3,\*</sup>

1 School of Mechanical, Medical and Process Engineering, Queensland University of Technology, Brisbane 4000, Australia

2 Centre for Biomedical Technologies, Queensland University of Technology, Brisbane 4000, Australia

3 School of Biological Science and Medical Engineering, Southeast University, Nanjing 210096, China

*All authors contributed equally to the manuscript*

## **\* Corresponding Author:**

Prof. Zhiyong Li

## **ABSTRACT**

Cardiovascular diseases (CVD) are the leading cause of morbidity and mortality worldwide. Atherosclerosis is the dominating underlying cause of CVD, that occurs at susceptible locations such as coronary and carotid arteries. The progression of atherosclerosis is a gradual process and most of the time asymptomatic until a catastrophic event occurs. Similarly, an intracranial aneurysm is the bulging of the cerebral artery due to a weakened area of the vessel wall. The progression of the aneurysm could result in the rupture of the vessel wall leading to a subarachnoid haemorrhage. The formation and progression of atherosclerosis and aneurysm are closely linked to abnormal blood flow behaviour and mechanical forces acting on the vessel wall. Recent technologies in medical imaging, modeling, and computation are used to estimate critical parameters from patient-specific data. However, there is still a need to develop protocols that are reproducible and efficient. This article focuses on the methods for biomechanical analysis of the cerebral aneurysms and atherosclerotic arteries including carotid & coronary. In this study, patient-specific 3D models were reconstructed from optical coherence imaging (OCT) for coronary and magnetic resonance imaging (MRI) for the carotid and cerebral arteries. The reconstructed models were used for computational fluid dynamics (CFD), structural-only, and fluid-structure interaction (FSI) simulations. The results of the FSI were compared against structural and CFD-only simulations to identify the most suitable method for each artery. The comparison between FSI and structural only simulations for the coronary artery showed similar mechanical stress values across the cardiac cycle with a maximum difference of 1.8%. However, the results for the carotid and cerebral arteries showed a maximum difference of 5% and 20% respectively. Additionally, with relation to the hemodynamic WSS calculated from FSI and CFD-only, the coronary artery presented a significant difference of 87%. Conversely, the results for the carotid and cerebral arteries showed a maximum difference of 9% and 6.4% at systole. Based on the results it can be concluded that the shape & location of the artery will influence the selection of the model that can be used for solving the numerical problem.

## KEYWORDS

Cardiovascular diseases; Computational biomechanics; Fluid-structure interaction; Cerebral aneurysm; carotid and coronary atherosclerosis; Wall shear stress; Principal stress

## INTRODUCTION

Cardiovascular disease (CVD) is an abnormal condition of the arteries that occurs at regions of disturbed blood flow due to sudden directional flow changes. CVD affects cerebral, coronary, carotid, iliac, renal, and femoral arteries. From a mechanical point of view, blood vessels are exposed to multiple kinds of mechanical forces, which are exerted on the vascular wall (radial, circumferential, and longitudinal forces) or the endothelial surface (shear stress). The stresses and strains experienced by arteries influence the initiation and progression of vascular diseases such as atherosclerosis and intracranial aneurysms. These diseases result in catastrophic events such as stroke and myocardial infarction (MI), the leading causes of morbidity and mortality globally. CVD accounted for approximately 42,300 deaths and 591,000 hospitalisations in Australia in the year 2019 (Health et al., 2021), and around 18.6 million deaths globally (Virani et al., 2021). CVD also have an impact on health care expenditure, costing around \$363.4 billion in the United States (Virani et al., 2021). In this regard, we will be presenting methodologies and results of the patient-specific biomechanical analysis of diseased arteries including coronary, carotid (atherosclerotic plaque), and cerebral (aneurysm) in separate sections with a focus on standardized approach and numerical techniques that could enable clinical implementation in the future.

Atherosclerosis is a chronic inflammatory disease characterized by hardening or narrowing of the arteries (Ross, 1999) in which plaque builds up underneath the endothelium, resulting in the partial or complete occlusion of arteries such as coronary and carotid. Plaque initiation, progression, and rupture are complex processes. Several factors like mechanical forces, plaque morphology, blood conditions, hypertension, living, and eating habits, influence the process (Morbiducci et al., 2016). Atherosclerotic plaque generally occurs at an arterial bend, characterized by flow separation and low shear stress (Chatzizisis et al., 2007). This disease develops at an early age and remains silent for decades. In the progression of atherosclerosis, lipid-filled macrophages are the major component. They undergo chemical changes, and the atherosclerotic plaque will become a combination of lipids, calcification, neovascularization, and possible haemorrhage. The center of the plaque, due to the deprivation of oxygen, can further develop into a necrotic core (Leiner et al., 2005). Currently, luminal narrowing is used as a marker for high-risk plaques; however, this is not an accurate estimator of plaque size, as this measurement underestimates the atherosclerotic burden (Adame et al., 2004).

Plaque stenosis severity, combined with patient-specific risk factors, is still the primary evaluation method used as guidance for treatment decisions related to atherosclerosis. This approach leaves behind patients with moderate stenosis, and such plaques can also be vulnerable. On the other hand, patients with stable plaques and a low risk of rupture are sent to surgery, and the surgery itself has some associated risks. Hence, an additional tool to evaluate the vulnerability of atherosclerotic plaques and cerebral aneurysms is needed, such as biomechanical computational analysis using patient-specific data. In this way, more drastic clinical events can be reduced and lower the number of unnecessary surgeries.

Another type of CVD is the intracranial aneurysm, which is the abnormal dilation of the arteries that is fragile and could rupture due to a stretched and thin wall at the aneurysm. According to our current understanding, intracranial aneurysm formation is a gradual process influenced by genetic, environmental, and hemodynamic risk factors (Etminan et al., 2016) resulting in vessel wall

degeneration, contributing to the structural remodelling and aneurysm growth (Sforza et al., 2009; Soldozy et al., 2019). Although the majority of aneurysms are small and are often asymptomatic (Williams et al., 2013), aneurysm rupture leads to subarachnoid haemorrhage resulting in significant morbidity and mortality (Brisman et al., 2006). Unruptured intracranial aneurysms (UIAs) develop over the life course remain unchanged for a long period before undergoing rapid growth and have an increased risk of rupture (Chien et al., 2013; Villablanca et al., 2013). Management of UIAs is currently based on risk stratification guidelines developed by large-scale clinical studies. These include PHASES (population, hypertension, age, size, earlier subarachnoid haemorrhage) score (Greving et al., 2014), UIATS (unruptured intracranial aneurysm treatment site) score (Etminan et al., 2015), and the ELAPSS (earlier subarachnoid haemorrhage, location of aneurysm, age, population, size, and shape) score (Backes et al., 2017). However, the accuracy of these scores is suboptimal due to the lack of considering quantitative factors.

Accurate information about plaque morphology and composition, aneurysm size/shape, and location in conjunction with the patient-specific flow conditions and risk factors are crucial to identify vulnerable plaques and aneurysms and the likelihood of their developing into cardiovascular events, such as stroke (Saam et al., 2005) and myocardial infarction. Non-invasive imaging modalities such as magnetic resonance imaging (MRI) and ultrasound (US) have been widely used in the characterization of carotid plaques. Other imaging techniques such as Computed Tomography (CT) and molecular imaging have also been used to a lesser extent due to the linkage with ionizing radiation. OCT is a state-of-the-art imaging technology, it could provide cross-sectional imaging of tissue morphology with high resolution ( $1\sim 15\ \mu\text{m}$  could be achieved) and in real-time (Dibildox et al., 2014; Fujimoto, 2001; Molina et al., 1998) for coronary arteries. In addition, the most used imaging modalities in the diagnosis, evaluation, and treatment of UIAs are, x-ray angiography, computed tomography angiography (CTA), and magnetic resonance angiography (MRA).

Vascular disease progression is associated with the biomechanical forces acting locally and the rupture is considered as a mechanical failure process. Therefore, biomechanics has the potential to evaluate plaque behaviour and predict its progression. For example, the morphological factors of a vulnerable plaque, such as a thin fibrous cap and large lipid core, will affect its mechanical behaviour, which in turn will be reflected by changes in biomechanical parameters. If a biomechanical parameter could be mapped to the current known clinical risk factors, it could be used as a biomechanical risk factor of plaque vulnerability. These biomechanical risk factors will give clinicians quantitative evidence to judge the plaque vulnerability, as an addition to the current imaging morphologies. Also, this has the potential ability to quantitatively predict the progression of the diseases, which is a supplement to current commonly used clinical risk factors.

Wall shear stress (WSS) and plaque structural stress (PSS) play a key role in the initiation and progression of atherosclerotic plaques. Hence, the evaluation of the biomechanical forces in specific geometries based on patient-specific medical imaging can give crucial insights into vulnerability. Computational analysis based on numerical methods such as the finite element method (FEM), finite volume method (FVM), finite difference method (FDM), Galerkin method, and spectral method, offer the possibility of evaluating these stresses (WSS and PSS) on specific artery geometries. The computational analysis combined with in-vivo medical imaging provides a less invasive and non-ionizing approach to identify the role of composition, morphology, and hemodynamic factors for understanding and treatment approach. In literature, various approaches such as computational fluid dynamics (CFD) (Gharahi et al., 2016; Liu et al., 2016; Mendieta et al., 2020; Xu et al., 2018; Zhao et al., 2000), structural stress analysis (Li et al., 2007; Li et al., 2006; Li et al., 2015; Paritala et al., 2021) and fluid-structure interaction (FSI) (Leach et al., 2010; Dalin Tang et al., 2017; Wang et al., 2020) are

used to understand the vascular biomechanics. In addition, from the literature, it is understood that local flow dynamics contribute to the initiation, growth, and rupture of atherosclerotic plaques and cerebral aneurysms (Asakura et al., 1990; Brown, Teng, Calvert, et al., 2016; Brown, Teng, Evans, et al., 2016) (Cebal et al., 2019; Cebal et al., 2011; Koskinas et al., 2009; Ku et al., 1983). Therefore image-based patient-specific computational simulations are widely used to understand the relationship between flow parameters and anatomical variations (Berg et al., 2019; Cebal et al., 2011; Lu et al., 2011; Steinman et al., 2003).

Even though multiple studies have explored the stresses exerted in the arteries due to blood flow, there is still a lack of understanding and standardization in analysing the stresses either by FSI or CFD simulation of the arteries. Therefore, this article focuses on comparing the FSI with CFD and structural simulations to understand if FSI is required or single physics can provide the same information with less computational expenses for certain models. It also presents a standard methodology for the reconstruction, meshing, setup, simulation, and analysis process for carotid, coronary, and aneurysm models. Application of standard methodology and process will improve confidence in the results and enable the development of a unified approach for analysing the stresses in the arteries. This study will be a step forward towards clinical application and provide crucial insights into the differences between single-physics and multi-physics models and when they should be used for three different arteries with a specific cardiovascular disease.

## MATERIALS AND METHODS

### Medical Imaging, Segmentation and 3D Reconstruction of Blood Vessels

#### Coronary arteries

The coronary study was based on OCT and angiography imaging data acquired from the Catheterization Laboratory in The Prince Charles Hospital (Chermside, QLD, Australia). In this study, a set of right coronary artery (RCA) imaging data from a 61-year-old male patient with acute coronary syndrome (ACS) was used. This study was approved by the internal review board and informed written consent was obtained.

The geometry for an FSI simulation contains both structure and fluid domains. From OCT the contours of the lumen and the plaque were obtained. As the intravascular-OCT is a catheter-based imaging modality, each contour must be stacked and aligned with the catheter path-line to form a 3D coronary model (Fig 1). This required 3D baseline could be generated from the angiography data, which was used as guidance during the OCT operation. Two plane angiographic images from two different directions were selected to generate the 3D baseline of the coronary artery. The central line of the coronary artery in each angiography imaging was segmented in ImageJ ([imagej.nih.gov/ij/](http://imagej.nih.gov/ij/)), the segmented central line was outputted as a set of 2D discrete point coordinates. The coordinates from the two plane angiography data were imported into SolidWorks (Dassault Systèmes, Vélizy-Villacoublay, France). In SolidWorks, these two splines in 2D planes were projected to form a new spline in 3D space. Finally, the 3D spline was discretized into a set of registration points and their 3D coordinates were exported. The number of points was determined by the corresponding OCT slice number. The OCT images were recorded in the axial direction during the pullback of a catheter in the coronary artery. Each slice provided a 2D view of the coronary lumen and vessel wall in the radial direction. In each slice, the contours of the lumen, the outer wall boundary, and plaque components were segmented by using ImageJ (Wang et al., 2020).

An in-house developed MATLAB (R2017a, MathWorks, Natick, MA, US) code package was used to register the 2D OCT contours onto the 3D angiographic baseline. The MATLAB code was designed to

have several functional packages, which contains all the sub-steps in the registration processes. Because of the difference in the resolution of the OCT and the angiography, the program firstly unified the scale of the point coordinates from the OCT and the angiography into the millimetre unit. Then in each OCT slice, the centroid was defined as the midpoint on the perpendicular bisector of the longest line segment between the two points on the lumen contour. Then each contour in each 2D OCT slice was moved to its position in 3D space by offsetting the centroid point onto the corresponding registration point on the 3D angiography baseline. Considering the tortuosity of coronary arteries, each OCT slice should be vertical against the local baseline curvature. A slope angle of each slice (from the normal vector of OCT slice plane to the local tangent vector of 3D baseline) was determined by calculating and applying a rotational matrix to each OCT slice. The transferred point coordinates were imported into the ANSYS SpaceClaim, a Geometry component in ANSYS Workbench (version 19.0, ANSYS, Canonsburg, PA, USA). Here the contours from each slice, including the coronary lumen, the outer boundary, and plaque component, were re-generated in a 3D space using the point coordinates. Then based on the contours, the surface of the coronary lumen, the outer wall, and the plaque were created separately by blending each kind of contours. Finally, the geometric model of the coronary lumen, the outer wall, and the plaque were generated by solidifying their surfaces and performing a Boolean operation on the overlapped parts between the outer wall, the lumen, and the plaque. To save the computational consumption, the coronary model was cut off so that only the part of the coronary model that we were interested in (the part with a plaque) was kept for the subsequent fluid-structure simulation, the length of the region of interest was approximately three times the length of the plaque.

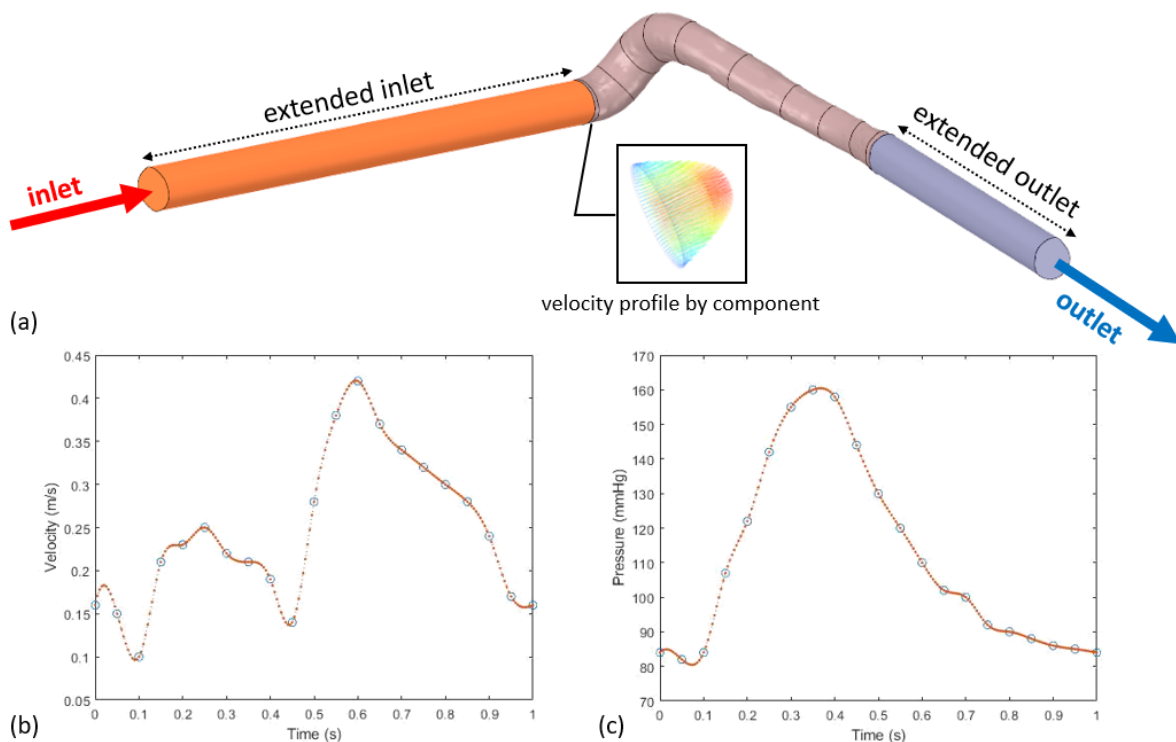


Fig 1. (a) Coronary artery geometry with extended inlet and outlet, and the box emphasized the fully developed flow profile defined by the velocity given as inlet to the FSI simulation. (b) velocity profile prescribed at the inlet, and (c) pressure profile given to the outlet.

### Carotid arteries

The study of the carotid atheroma was based on Magnetic Resonance Imaging (MRI), part of research approved by the Human Research Ethics Committee at the Princess Alexandra Hospital (PAH) in

Brisbane, Australia, and by the Queensland University of Technology's (QUT) Office of Research Ethics and Integrity (HREC/17/QPAH/181). The multi-contrast MR imaging study was performed on a Magnetom Prisma (Siemens Medical Solutions, Malvern, PA, USA) 3T MR whole body system using a 64-channel head/neck coil. Four MRI contrast weighted imaging techniques were employed. The parameters used were T2-weighted (TR 4040 msec, TE 89 msec, resolution 456 x 384 x 40, FOV 213 x 180), proton density (PD) (TR 2720 msec, 29 msec, resolution 384 x 384 x 40, FOV 180 x 180), T1-weighted (TR 717 msec, 9.9 msec, resolution 320 x 320 x 40, FOV 180 x 180), and Time of Flight (TOF) (TR 21msec, TE 3.11msec, resolution 384 x 290 x 136, FOV 151 x 199). Additionally, 2D ECG-gated phase-contrast MRI (PC-MRI) images were acquired at three different locations (common carotid artery (CCA), maximum stenotic region, and internal carotid artery (ICA)). The scan parameters were TR 24.36msec, TE 3.59msec, resolution 240 x 240, FOV 111 x 111; velocity encoding (VENC) ranging from 60 cm·s<sup>-1</sup> to 100 cm·s<sup>-1</sup>.

One patient with identified carotid stenosis (>90% based on Ultrasound (US) doppler) was scanned using MRI before carotid endarterectomy (CEA), and written consent was obtained before scanning. The patient-specific 3D geometry segmentation and reconstruction were developed using our previously established protocol (Gao et al., 2009; Mendieta et al., 2020; Wang et al., 2020). In brief, T1 was employed to identify the plaque components focused on lipids, calcification, and arterial wall using Amira (version 6.0, FEI, Hillsboro, Oregon, USA). T2, PD, and TOF were utilised as supporting sequences for component identification. The mass flow rate was extracted from PC-MRI which also was employed in FSI analysis as an inlet at the CCA. The pressure applied to the internal region in the 3D structural-only analysis was calculated using the patient-specific pressure-arm scaled based on the mass flow rate profile. For FSI analysis this pressure was utilised as outlets at the ICA and ECA (Fig 2). A mesh independent test was performed to identify the adequate element size for both methods, structural and fluid parts.

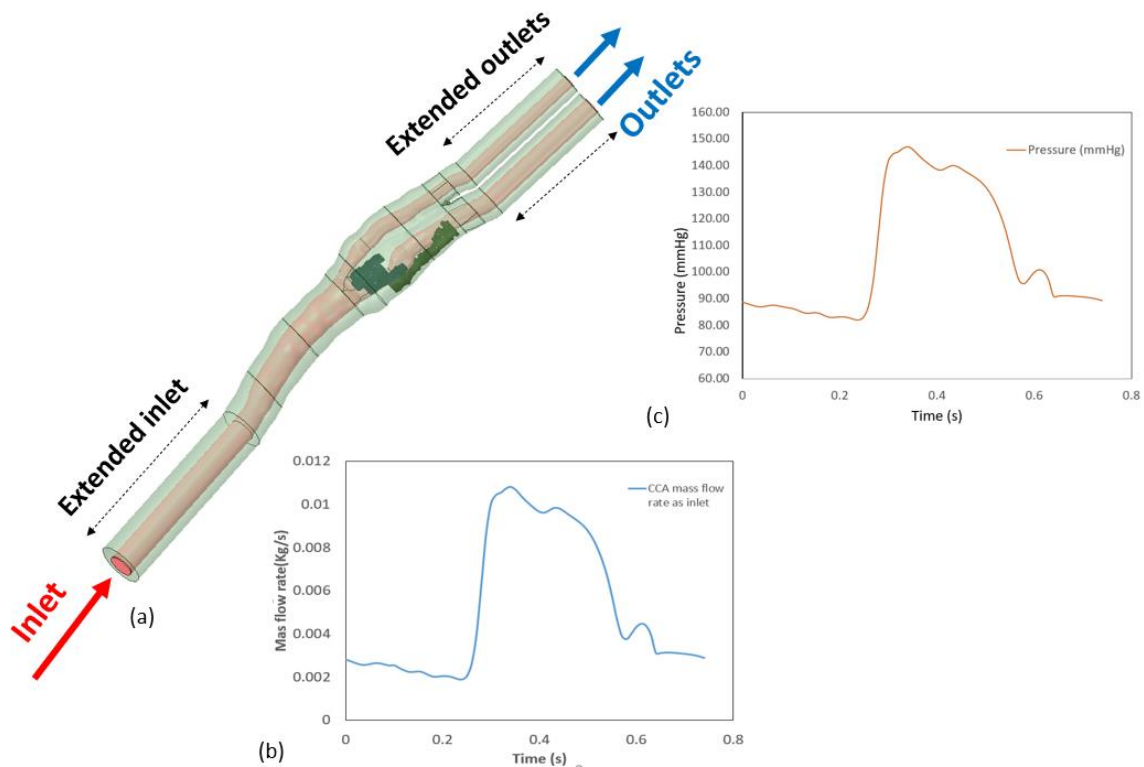


Fig 2. (a) Carotid artery geometry including plaque components (lipids and calcification) with extended inlet and outlets. (b) Mass flow rate profile given as inlet, (c) pressure profile given at the outlets.

#### Cerebral arteries

For the study of a cerebral artery, the data from a patient with identified middle cerebral artery (MCA) aneurysm was employed. The data included, Time of Flight (TOF) MRA and T1 scans for imaging the unruptured cerebral aneurysm. The parameters used were T1-weighted (TR 2.5 msec, TE 0.95 msec, resolution 315 x 96 x 360, FOV 308 x 352), and Time of Flight (TOF) (TR 1000 msec, TE 15 msec, resolution 320 x 320 x 240, FOV 320 x 320). The multi-contrast imaging study was performed on a Magnetom Prisma (Siemens Medical Solutions, Malvern, PA, USA) 7T MR whole body system. Time-of-flight (TOF) magnetic resonance angiograms (MRA) and T1 of sequences were imported into an image processing software package, Amira (version 6.0, FEI, at Hillsboro, Oregon, USA). The region of interest corresponding to the MCA aneurysm was segmented using a thresholding technique for 3D reconstruction of the aneurysm lumen and the parent vessels. For the arterial wall, manual segmentation was performed to identify the non-uniform thickness of the wall (Fig 3). The initial geometries created from Amira were smoothed using an open-source software Meshmixer 3.5 (2020 Autodesk, Inc) to improve the quality of the reconstruction by increasing the element density of the construction for better CFD outcomes.

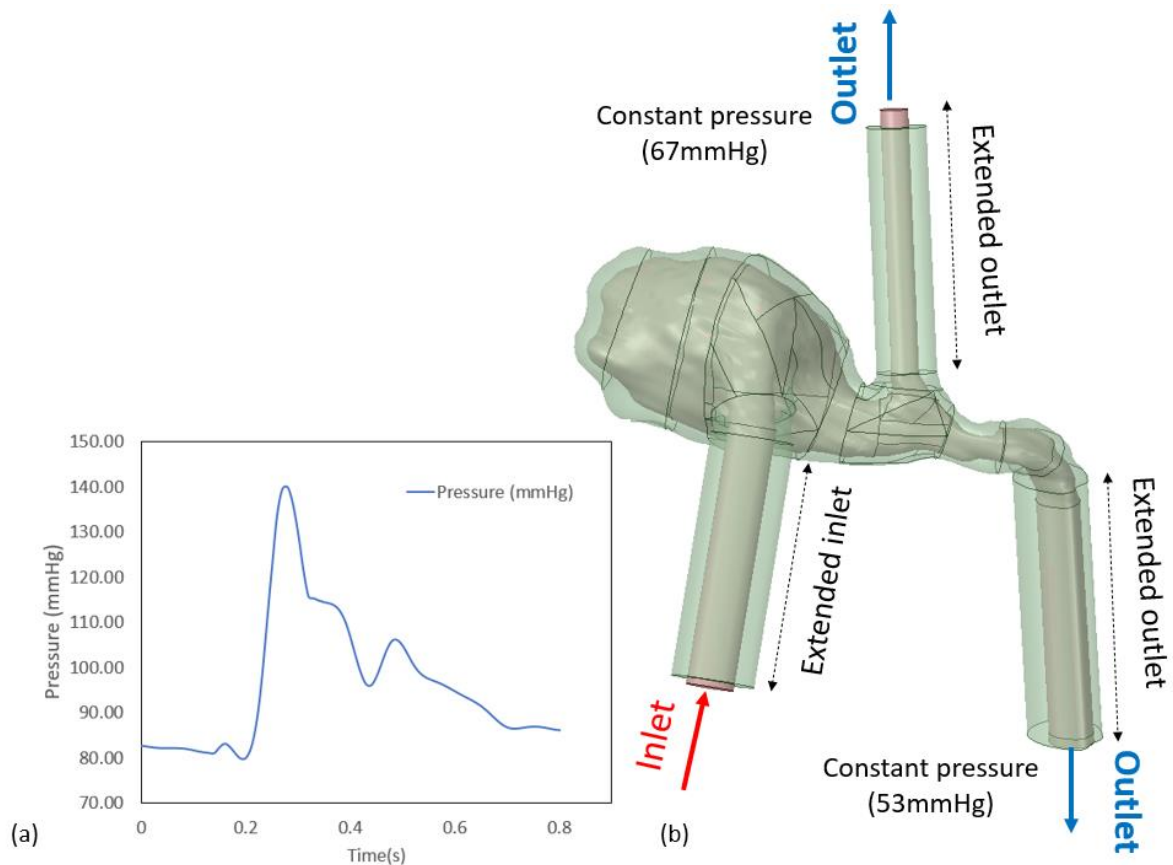


Fig 3. (a) Pressure profile given to the inlet, and (b) middle cerebral artery geometry with extended inlets and outlets, showing the constant pressure used at the outlets.

## Computational Analysis

### Structural computational model

The different plaque components (calcification and lipids) and arterial wall for the three models were meshed using the proximity and curvature function size with default element size and discretized with tetrahedral elements. The number of elements generated for each geometry were 890158, 811375, and 1241307 for the coronary, carotid, and aneurysm models respectively. Extensions were also added to the ends of the models to match the length of the fluid domain and allow a fully developed flow to reach the region of interest (atheroma or aneurysm). Fixed support was added to the narrow edges of the geometries at the ends of the extensions. The material properties for the vessel wall and plaque components were assumed to be isotropic elastic, with Poisson's ratio of 0.48 for all materials and Young's Modulus of 10MPa for calcification, 0.02MPa for lipids, and 0.6MPa for arterial tissue (Benitez et al., 2021; Gao et al., 2009; Mendieta et al., 2020; Paritala et al., 2021). In the aneurysm, the material properties of the vessel wall were assumed as, Poisson's ratio of 0.48 and Young's Modulus of 3MPa. The Young's modulus of cerebral aneurysms has values between approximately 0.5-5.7MPa (Cebal et al., 2015).

### Fluid computational model

For all cases, blood flow was assumed to be laminar incompressible, homogenous, and Newtonian, with a viscosity of 0.00345 Pa·s and a density of 1050kg/m<sup>3</sup>. In the FSI simulation, the dynamic mesh function had to be enabled for the fluid domain with the diffusion and remesh functions with an interval of 1. This function allowed the motion of the boundary in the fluid participant and transfer

the fluid pressure to the structural part of the FSI. Adaptive mesh with tetrahedral elements with a coarse size of 0.30 mm was selected for the fluid part. Also, inflation was added to the fluid domain boundary, 5-layer to the coronary model, and 10-layer to the carotid and aneurysms models. This mesh setup guaranteed there was no negative cell volume error when performing FSI simulation with a relatively big time step of 0.01s for CFD and FSI for all the geometries. The number of elements generated for each geometry were 80534, 641749, and 1382850 for the coronary, carotid, and aneurysm models respectively. The interior of the lumen and the geometry were set as deforming dynamic zones and the wall was set as a system coupling zone.

#### Boundary conditions and co-simulation settings

For the coronary artery, a time-dependent velocity boundary condition was prescribed at the inlet and a time-dependent pressure boundary condition was given at the outlet. The original waveforms were acquired from wave intensity analysis (Broyd et al., 2017), based on the number of time points in the FSI simulation, the velocity and pressure waveforms were interpolated to a set of discrete points. As the geometry we used for the FSI simulation was only a short section of the full-long coronary model, the blood flow was not able to fully develop from the inlet. A CFD-only model with extended inlet and outlet was performed to obtain fully developed parabolic flow velocity profiles used as the boundary condition for the subsequent FSI simulation. Later the velocity profiles defined by element coordinates and velocity components were directly given to the inlet of the fluid domain in the FSI simulation (Fig 1). By using the extended CFD-only model, it helped to get the flow profile fully developed in the meanwhile saving a huge computational consumption in FSI simulation.

In the carotid artery model, patient-specific mass flow rate waveforms were computed using Segment (version 2.2, Medviso, R6435, Lund, Sweden) by selecting the region corresponding to the lumen of the CCA, in the PC-MRI images and integrating the axial velocity (further information can be found in our previous study). Arm blood pressure was also acquired for the patient. The diastolic and systolic pressure values were scaled to the mass flow rate profile. Fig 2 shows the boundary conditions in terms of pressure (as outlets at the ICA and ECA) and mass flow rate (as inlet at the CCA) profiles used for the FSI calculation as an example. Fig 2 also shows the resolved mass flow rate (MFR) at the ICA and ECA by FSI. In the aneurysm model, a time-dependent pulsatile pressure profile was defined at the inlet (MCA) and the constant pressure of 8000 and 9000 Pa was defined at the outlets. The prescribed pressure profile (80-120mmHg) corresponds to normal blood pressure (Fig 3).

CFD, structural, and FSI simulations were performed on ANSYS Workbench (explicit formulation) platform using the finite volume for the fluid simulation and finite element method for the structural. The time step for all the simulations was 0.01s. The same computational power was allowed to the multi-physics and single-physics simulations (24 CPUs to the fluid participant and 8 CPUs to the structural participant). System Coupling component was used for controlling pressure/force and displacement data transferring between the two participants (Fluent and transient structural). For data transfer, the inner surface of the structural part which is in contact with the lumen was set as the fluid-solid interface. No-slip conditions and normal stress equilibrium conditions were assumed at all interfaces. The timestep in system coupling was set to 0.01s, running for two cardiac cycles. At each timestep, the values of transferring data were ramped linearly in the first 5 coupling iterations (minimum iteration number) to help in the stability of the coupled simulation. To avoid instability of the results from the initial time steps, only the data from the second cycle were used for post-processing.

## Data Analysis

To compare our FSI model with conventional structural-only, and CFD-only simulations we used the same geometry from FSI simulations. In the conventional transient structural analysis, the fluid-structure interface on the inner surface of the arterial wall was replaced by direct pressure waveform load, while other settings were kept the same as in the FSI simulation. Principal stress (stress-P1) was compared from both simulations at one location for all the time points. Stress-P1 provides information related to the normal stress at an angle on a plane where shear stress is zero. In the CFD-only simulation, the same setting was given as in the FSI model but the dynamic mesh and the system coupling interface were disabled. Wall shear stress (WSS) distribution was compared from CFD only and FSI results, using the area at which the WSS is lower than 2Pa for the coronary and carotid arteries, and 10 Pa for the cerebral artery. The analysis was performed at systole for all the geometries.

## RESULTS

### Coronary Artery

#### Principle stress comparison from structural and FSI simulations

By comparing the stress-P1 results related to the coronary artery, it was found that the values are close to each other from the FSI and structural only simulation. This information can be verified from Fig 4, where the maximum difference was 820 Pa (1.8%) found after systole. Additionally, both curves followed the same trend as the pressure profile, prescribed as a boundary condition.

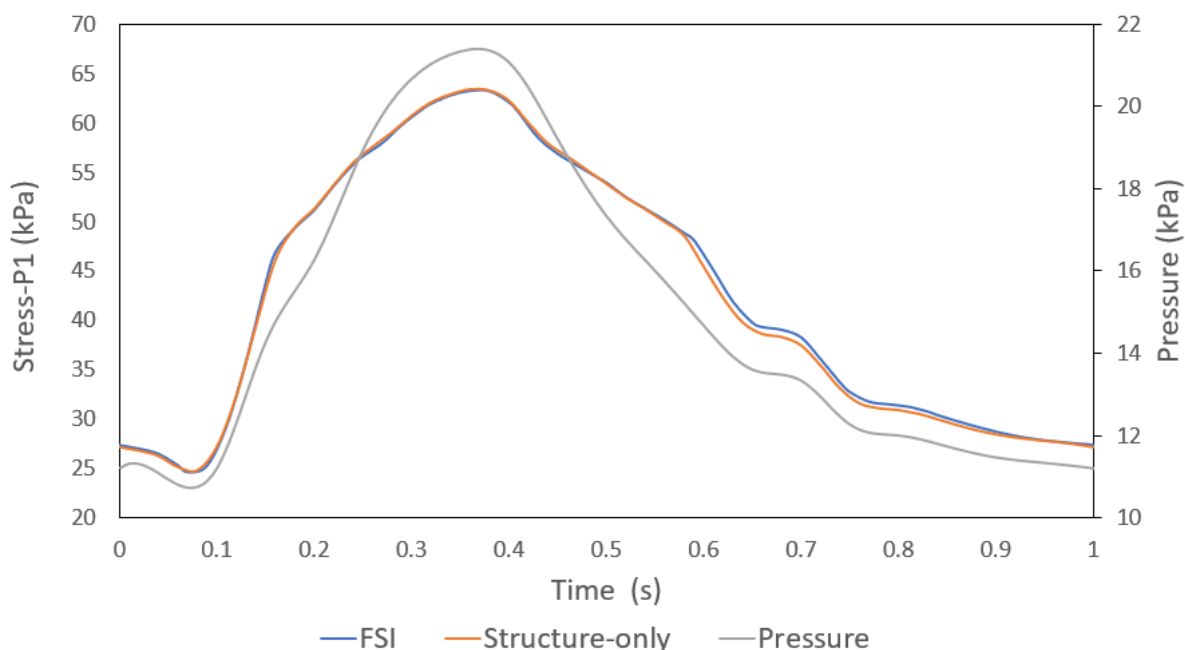


Fig 4. Comparison of the principal stress (Stress-P1) between FSI and structural-only simulations of the coronary artery at a specific selected point. The plot also illustrates the pressure profile prescribed for calculation.

#### Wall shear stress analysis and comparison from CFD and FSI simulations

Fig 5 (a and b) shows the WSS contours at the 0.8s time point, for FSI and CFD-only simulations. Additionally, Fig 5(c) illustrates the change in area with lower than 2Pa across the complete cardiac cycle. From there, it can be seen that CFD-only simulation tended to provide lower values than the FSI simulation due to the non-deformable rigid wall. The maximum difference between the area of the low WSS for FSI and CFD simulations was 87%. FSI model detected more area for low WSS because the fluid domain could expand circumferentially when pressure loaded to the flexible arterial wall. Also, the area with low WSS correlates negatively to the velocity flow wave.

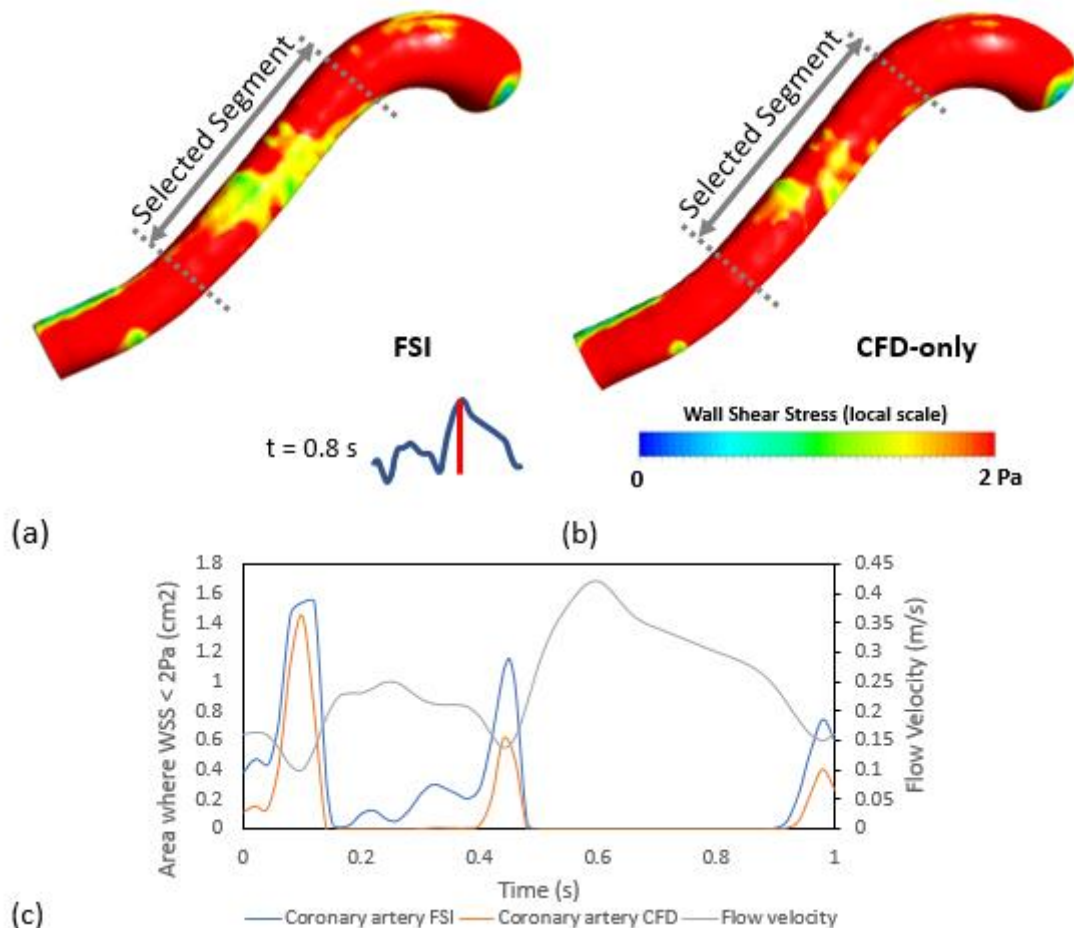


Fig 5. Contours of  $WSS < 2Pa$  at the 0.8s time point, for (a) the FSI and (b) CFD-only simulations. (c) Shows the area within the coronary luminal geometry with  $WSS < 2Pa$  across the cardiac cycle.

## Carotid Artery

Principle stress comparison from structural and FSI simulations

Stress-P1 was also investigated for the carotid arteries at a specific location within the carotid plaque at the level of the bifurcation. Fig 6 shows that FSI simulation tended to provide higher values than CFD-only and was more noticeable at the region of systole in the cardiac cycle. The maximum difference located at systole was 1.25 kPa which is about 5%. However, both curves followed the trend given by the prescribed pressure profile.

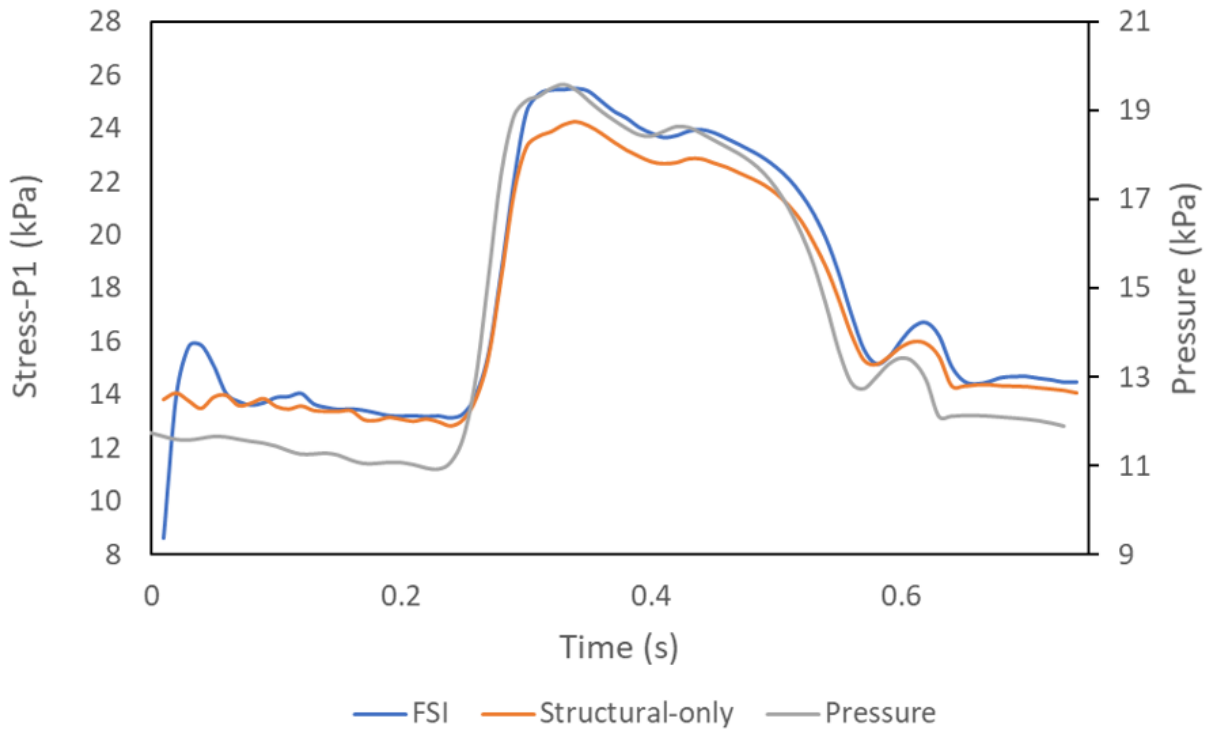


Fig 6. Comparison of the principal stress (Stress-P1) between FSI and structural-only simulations of the carotid artery at a specific selected point. The plot also illustrates the pressure profile prescribed for calculation.

#### Wall shear stress analysis and comparison from CFD and FSI simulations

Fig 7 (a and b) illustrates the low WSS contours from the CFD-only and FSI simulation for the carotid artery geometry, at the 0.34s time point of the cardiac cycle. FSI analysis also provided higher areas across the cardiac cycle compared to CFD-only simulation (Fig 7(c)) with a maximum difference of 9%. For this geometry, it is observed that the data from FSI simulation shifted to the right compared to CFD-only. Even though there is a clear difference between both sets of data, both curves followed a negatively correlated pattern with relation to the mass flowrate prescribed as a boundary condition.

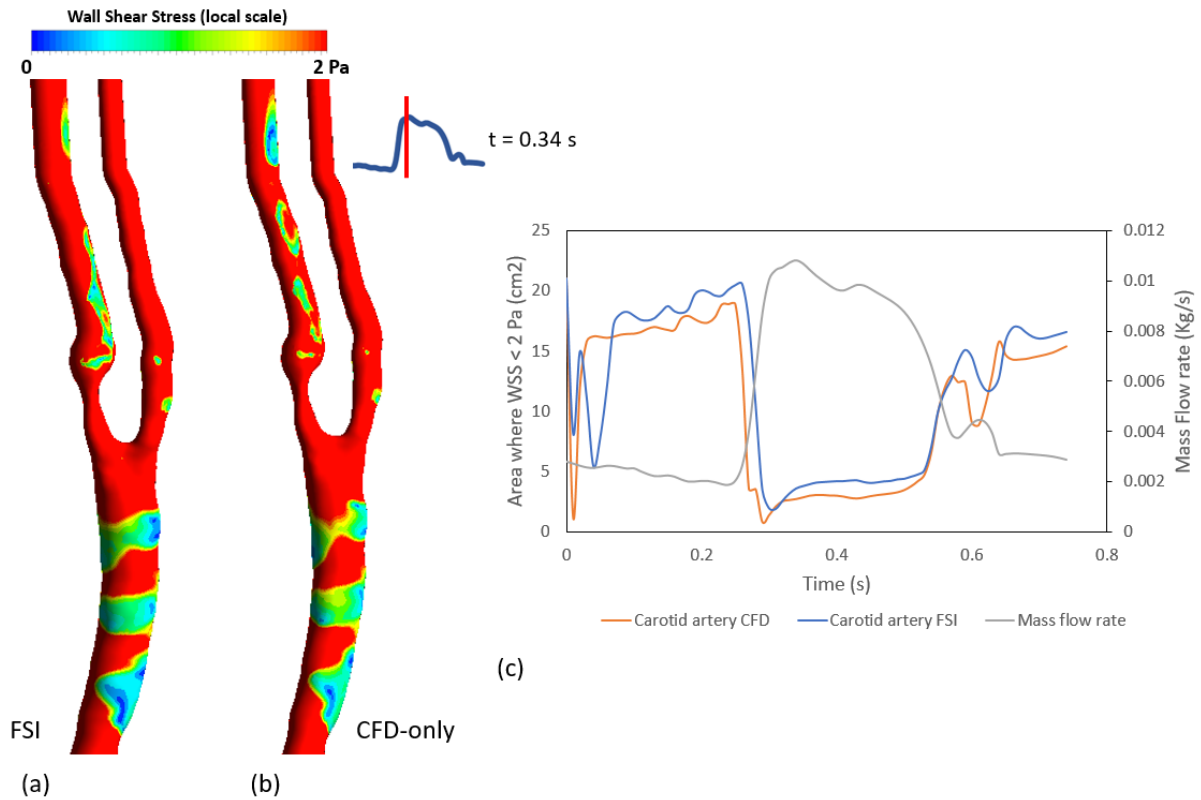


Fig 7. Contours of WSS < 2Pa at the 0.34s time point, for (a) the FSI and (b) CFD-only simulations. (c) shows the area within the carotid luminal geometry with WSS < 2Pa across the cardiac cycle.

## Cerebral Artery

Principle stress comparison from structural and FSI simulations

Fig 8 provides the summary of the data related to the stress-P1 collected for the cerebral artery for the structural-only and FSI simulation, at the thinnest region of the arterial wall. The data presents a consistent difference across the cardiac cycle with a maximum difference of 30kPa (20%), at systole. Both curves also followed the trend given by the pressure profile used as a boundary condition.

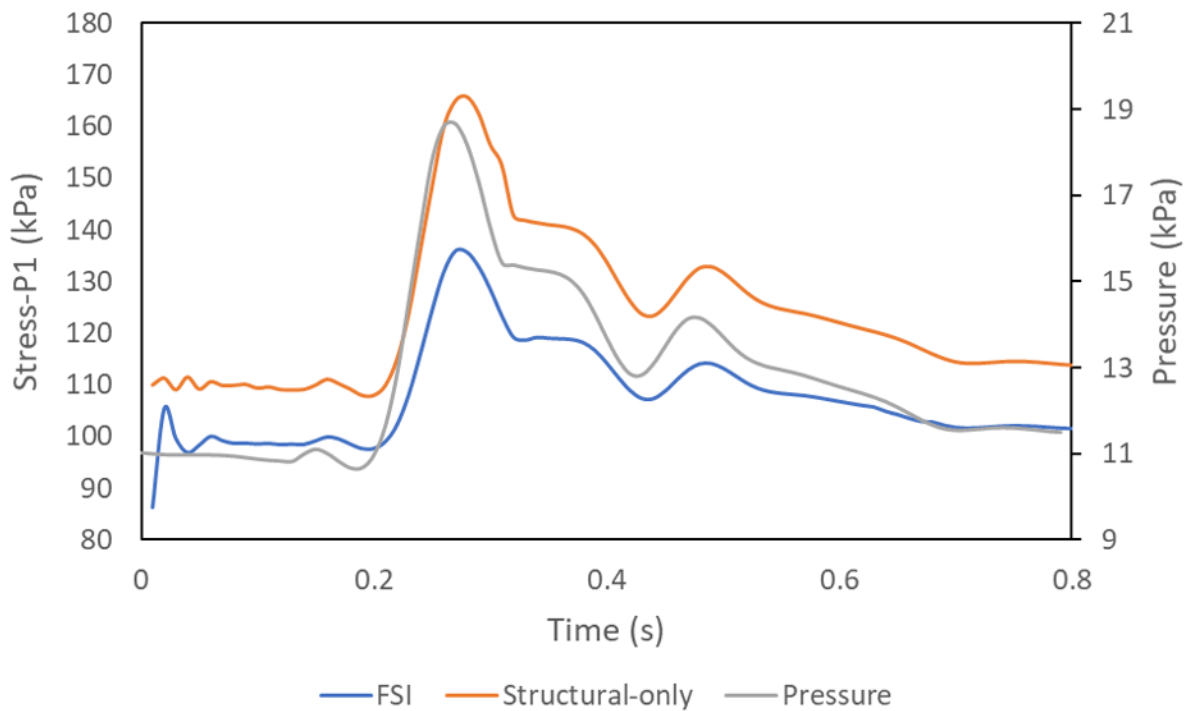


Fig 8. Comparison of the principal stress (Stress-P1) between FSI and structural-only simulations of the cerebral artery at a specific selected point. The plot also illustrates the pressure profile prescribed for calculation.

#### Wall shear stress analysis and comparison from CFD and FSI simulations

The contours from the FSI and CFD-only simulations plotted at systole (0.28s) are shown in Fig 9(a and b), with a maximum value of 10 Pa. Additionally, Fig 9(c) presents the area of WSS lower than 10 Pa. For the cerebral artery, it is observed that both FSI and CFD-only analysis provided almost identical values across the cardiac cycle, with a maximum difference of 6.4%. The data provided by the FSI and CFD-only analysis provided a negative correlation to the pressure profile prescribed as a boundary condition.

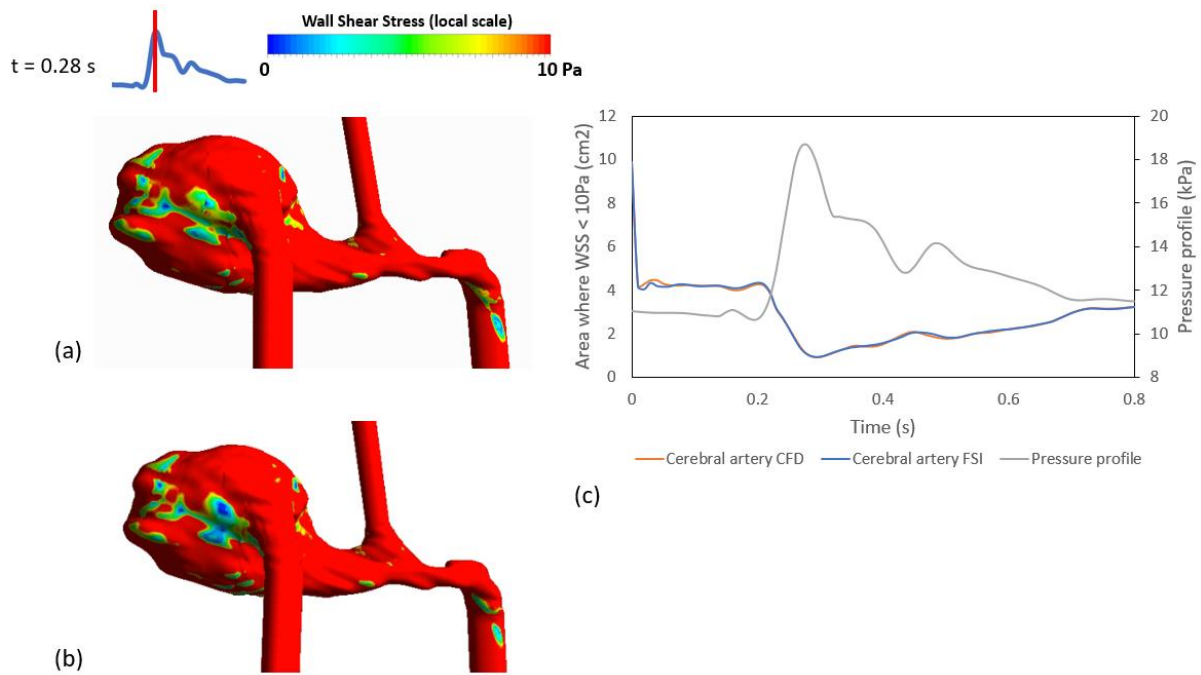


Fig 9. Contours of WSS < 2Pa at the 0.28s time point, for (a) the FSI and (b) CFD-only simulations. (c) shows the area within the cerebral luminal geometry with WSS < 2Pa across the cardiac cycle.

## DISCUSSION

Overall, the three investigated arteries presented different patterns, for example with relation to the comparison from the structural-only and FSI simulation, the coronary artery showed similar values across the cardiac cycle, contrary to the carotid and cerebral arteries. For these arteries, there was a noticeable difference across the cardiac cycle. This may be due to the characteristics of each model. In the case of the coronary artery, the model included lipids as a plaque component, for the carotid artery the model included lipid and calcification, for the cerebral artery the model had just the arterial tissue and the highest stress was in the thinnest region of the wall. However, in all cases, the results from the simulations followed the trend prescribed by the pressure profile set as a boundary condition. It is also important to mention that in a structural-only simulation the pressure is applied homogeneously to the internal wall of the structure, instead in the FSI simulation the force is given node by node by the CFD calculation.

With relation to the area at low WSS calculated for the different geometries from FSI and CFD-only simulations, the coronary and the carotid artery presented the significant difference between the values compared to the cerebral artery where the values are highly close to each other. This pattern can be due to the material properties given to the arterial wall for each simulation. For example, in the case of the coronary and carotid artery, even though the models included plaque component lipids and calcification, the arterial wall was defined with Young's modulus of 0.6MPa instead in the cerebral artery Young's modulus was 3MPa. This value was selected due to the complexity of the geometry which allowed the acquisition of the FSI data.

Two different imaging modalities were used in this study to extract the geometries for simulation. In the case of the coronary artery the geometry was extracted from OCT, and for the carotid and cerebral arteries, the geometries were extracted from MRI. This information provides the basic framework for further studies that aimed to segment and 3D reconstructed models for FSI, structural, and CFD only simulations.

Table 1. Computational time consumption for each geometry and method using 24 CPUs for the CFD and 8 CPUs for the structural participant.

Computational time	FSI	Structural-only	CFD-only
Coronary	17h39m	2h50m	45m
Carotid	41h50m	2h4m	1h3m
Cerebral	171h	7h40m	4h25m

FSI is a valuable tool that can provide information in terms of structural and CFD analysis of a specific geometry. However, it is computationally expensive and time-consuming (Table 1), and in some cases, it may not reach convergence due to the complexity of the models. Therefore, this study compared the results of CFD and structural only simulations against FSI simulations to identify if single-physics can provide similar information as the multi-physics approach. In the case of the coronary artery, for the structural-FSI comparison there was a small difference in terms of deformation and stress. However, the comparison between CFD and FSI simulations showed a clear difference in WSS values indicating that FSI is still required. For the carotid artery, both comparisons (structural-FSI and CFD-FSI) presented different values to each other, which suggests that for this geometry and settings there is still a necessity for the information provided by FSI. In the case of the cerebral artery, the structural-FSI comparison presented the highest difference in stress values, contrary to the CFD-FSI comparison which showed similar results. This information suggests that FSI will be needed for the structural participant of the cerebral artery. In summary, it was observed that the results from CFD, structural and FSI simulations were influenced by the type of geometry evaluated, and simulation settings.

### Limitations

The results of the numerical simulations are based on the geometry of the model, the loads or boundary conditions employed, and the material properties. In this study, the geometry and the boundary conditions are patient-specific for the carotid artery; however, the material properties and the boundary conditions for the coronary and cerebral arteries are still based on previous studies (Paritala et al., 2018; Wang et al., 2020), where a linear elastic behaviour was assumed for the arterial tissue, calcification, and lipids. Further investigation is required with relation to non-linear elastic material properties to the plaque components using the proposed methods.

Another limitation of this study is that the shrinkage or zero-state pressure procedure was not performed in the geometries. Some studies have performed it using a uniform circumferential shrink and axial stretch ratio (Huang et al., 2009; D. Tang et al., 2017). Even though this procedure is valuable, it was demonstrated previously that applying a method to address this issue, will not affect the results significantly (Benitez et al., 2021), instead will increase the complexity of the models.

The proposed methods were only applied to one patient per location (coronary, carotid, and cerebral arteries). Future larger-scale patient studies are needed to further demonstrate the feasibility and advantage of the methods. It is also recognised that experimental validation can give further insight into the accuracy of the results.

## CONCLUSIONS

This article presented the methods for biomechanical analysis of coronary, carotid, and cerebral arteries. The results for the hemodynamic, mechanical, and FSI simulations were compared to understand the applicability of single and multi-physics methods for different arteries. For the coronary artery, the results of the structural-only and FSI simulations were in agreement, whereas CFD-only results were significantly different from the FSI simulations. The results for the CFD-only and

structural-only against FSI simulations were comparable for the carotid artery. In the cerebral artery, the comparison between structural-only against FSI simulations presented substantial differences, whereas CFD-only and FSI simulation results were in agreement. In conclusion, the shape, location of an artery, and simulation settings should be considered when selecting a computational model. Further large-scale studies are required to verify the results and propose a method for different arteries.

## References

- Adame, I., Van Der Geest, R., Wasserman, B., Mohamed, M., Reiber, J., Lelieveldt, B. J. M. R. M. i. P., Biology, & Medicine. (2004). Automatic segmentation and plaque characterization in atherosclerotic carotid artery MR images. *16*(5), 227-234.
- Asakura, T., & Karino, T. J. C. r. (1990). Flow patterns and spatial distribution of atherosclerotic lesions in human coronary arteries. *66*(4), 1045-1066.
- Backes, D., Rinkel, G. J., Greving, J. P., Velthuis, B. K., Murayama, Y., Takao, H., . . . Jääskeläinen, J. E. J. N. (2017). ELAPSS score for prediction of risk of growth of unruptured intracranial aneurysms. *88*(17), 1600-1606.
- Benitez, J., Fontanarosa, D., Wang, J., Paritala, P. K., McGahan, T., Lloyd, T., & Li, Z. (2021). Evaluating the Impact of Calcification on Plaque Vulnerability from the Aspect of Mechanical Interaction Between Blood Flow and Artery Based on MRI. *Annals of Biomedical Engineering*, *49*(4), 1169-1182. doi:10.1007/s10439-020-02655-1
- Berg, P., Voß, S., Janiga, G., Saalfeld, S., Bergersen, A. W., Valen-Sendstad, K., . . . surgery. (2019). Multiple Aneurysms AnaTomy CHallenge 2018 (MATCH)—phase II: rupture risk assessment. *14*(10), 1795-1804.
- Brisman, J. L., Song, J. K., & Newell, D. W. J. N. E. j. o. m. (2006). Cerebral aneurysms. *355*(9), 928-939.
- Brown, A. J., Teng, Z., Calvert, P. A., Rajani, N. K., Hennessy, O., Nerlekar, N., . . . Hoole, S. P. J. C. C. I. (2016). Plaque structural stress estimations improve prediction of future major adverse cardiovascular events after intracoronary imaging. *9*(6), e004172.
- Brown, A. J., Teng, Z., Evans, P. C., Gillard, J. H., Samady, H., & Bennett, M. R. J. N. r. c. (2016). Role of biomechanical forces in the natural history of coronary atherosclerosis. *13*(4), 210-220.
- Broyd, C. J., Davies, J. E., Escaned, J. E., Hughes, A., & Parker, K. (2017). Wave intensity analysis and its application to the coronary circulation. *Global cardiology science & practice*, *2017*(1), e201705-e201705. doi:10.21542/gcsp.2017.5
- Cebral, J. R., Detmer, F., Chung, B. J., Choque-Velasquez, J., Rezai, B., Lehto, H., . . . Yu, A. J. A. J. o. N. (2019). Local hemodynamic conditions associated with focal changes in the intracranial aneurysm wall. *40*(3), 510-516.
- Cebral, J. R., Duan, X., Chung, B. J., Putman, C., Aziz, K., & Robertson, A. J. A. J. o. N. (2015). Wall mechanical properties and hemodynamics of unruptured intracranial aneurysms. *36*(9), 1695-1703.
- Cebral, J. R., Mut, F., Weir, J., & Putman, C. M. J. A. J. o. N. (2011). Association of hemodynamic characteristics and cerebral aneurysm rupture. *32*(2), 264-270.
- Chatzizisis, Y. S., Coskun, A. U., Jonas, M., Edelman, E. R., Feldman, C. L., & Stone, P. H. J. J. o. t. A. C. o. C. (2007). Role of endothelial shear stress in the natural history of coronary atherosclerosis and vascular remodeling: molecular, cellular, and vascular behavior. *49*(25), 2379-2393.
- Chien, A., Liang, F., Sayre, J., Salamon, N., Villablanca, P., & Viñuela, F. J. J. o. n. (2013). Enlargement of small, asymptomatic, unruptured intracranial aneurysms in patients with no history of subarachnoid hemorrhage: the different factors related to the growth of single and multiple aneurysms. *119*(1), 190-197.

- Dibildox, G., Baka, N., Punt, M., Aben, J. P., Schultz, C., Niessen, W., & van Walsum, T. J. M. p. (2014). 3D/3D registration of coronary CTA and biplane XA reconstructions for improved image guidance. *41*(9), 091909.
- Etminan, N., Brown, R. D., Beseoglu, K., Juvela, S., Raymond, J., Morita, A., . . . Mocco, J. J. N. (2015). The unruptured intracranial aneurysm treatment score: a multidisciplinary consensus. *85*(10), 881-889.
- Etminan, N., & Rinkel, G. J. J. N. R. N. (2016). Unruptured intracranial aneurysms: development, rupture and preventive management. *12*(12), 699-713.
- Fujimoto, J. G. (2001). Optical coherence tomography. *Comptes Rendus de l'Académie des Sciences - Series IV - Physics*, *2*(8), 1099-1111.
- Gao, H., Long, Q., Graves, M., Gillard, J. H., & Li, Z. Y. (2009). Carotid arterial plaque stress analysis using fluid-structure interactive simulation based on in-vivo magnetic resonance images of four patients. *J Biomech*, *42*(10), 1416-1423. doi:10.1016/j.jbiomech.2009.04.010
- Gharahi, H., Zambrano, B. A., Zhu, D. C., DeMarco, J. K., Baek, S. J. I. j. o. a. i. e. s., & mathematics, a. (2016). Computational fluid dynamic simulation of human carotid artery bifurcation based on anatomy and volumetric blood flow rate measured with magnetic resonance imaging. *8*(1), 46-60.
- Greving, J. P., Wermer, M. J., Brown Jr, R. D., Morita, A., Juvela, S., Yonekura, M., . . . Rinkel, G. J. J. T. L. N. (2014). Development of the PHASES score for prediction of risk of rupture of intracranial aneurysms: a pooled analysis of six prospective cohort studies. *13*(1), 59-66.
- Health, A. I. o., & Welfare. (2021). *Heart, stroke and vascular disease—Australian facts*. Retrieved from Canberra: <https://www.aihw.gov.au/reports/heart-stroke-vascular-diseases/hsvd-facts>
- Huang, X., Yang, C., Yuan, C., Liu, F., Canton, G., Zheng, J., . . . Tang, D. (2009). Patient-specific artery shrinkage and 3D zero-stress state in multi-component 3D FSI models for carotid atherosclerotic plaques based on in vivo MRI data. *Molecular & cellular biomechanics : MCB*, *6*(2), 121-134.
- Koskinas, K. C., Chatzizisis, Y. S., Baker, A. B., Edelman, E. R., Stone, P. H., & Feldman, C. L. J. C. o. i. c. (2009). The role of low endothelial shear stress in the conversion of atherosclerotic lesions from stable to unstable plaque. *24*(6), 580-590.
- Ku, D. N., & Giddens, D. P. (1983). Pulsatile flow in a model carotid bifurcation. *Arteriosclerosis: An Official Journal of the American Heart Association, Inc.*, *3*(1), 31-39.
- Leach, J. R., Rayz, V. L., Soares, B., Wintermark, M., Mofrad, M. R., & Saloner, D. J. A. o. b. e. (2010). Carotid atheroma rupture observed in vivo and FSI-predicted stress distribution based on pre-rupture imaging. *38*(8), 2748-2765.
- Leiner, T., Gerretsen, S., Botnar, R., Lutgens, E., Cappendijk, V., Kooi, E., & Van Engelshoven, J. J. E. r. (2005). Magnetic resonance imaging of atherosclerosis. *15*(6), 1087-1099.
- Li, Z.-Y., Howarth, S., Tang, T., Graves, M., Jean, U., & Gillard, J. H. J. C. d. (2007). Does calcium deposition play a role in the stability of atheroma? Location may be the key. *24*(5), 452-459.
- Li, Z.-Y., Howarth, S., Trivedi, R. A., U-King-Im, J. M., Graves, M. J., Brown, A., . . . Gillard, J. H. J. J. o. b. (2006). Stress analysis of carotid plaque rupture based on in vivo high resolution MRI. *39*(14), 2611-2622.
- Li, Z.-Y., Tan, F. P., Soloperto, G., Wood, N. B., Xu, X. Y., Gillard, J. H. J. C. m. i. b., & engineering, b. (2015). Flow pattern analysis in a highly stenotic patient-specific carotid bifurcation model using a turbulence model. *18*(10), 1099-1107.
- Liu, X., Zhang, H., Ren, L., Xiong, H., Gao, Z., Xu, P., . . . Physiology, C. (2016). Functional assessment of the stenotic carotid artery by CFD-based pressure gradient evaluation. *311*(3), H645-H653.
- Lu, G., Huang, L., Zhang, X., Wang, S., Hong, Y., Hu, Z., & Geng, D. J. A. J. o. N. (2011). Influence of hemodynamic factors on rupture of intracranial aneurysms: patient-specific 3D mirror aneurysms model computational fluid dynamics simulation. *32*(7), 1255-1261.

- Mendieta, J. B., Fontanarosa, D., Wang, J., Paritala, P. K., McGahan, T., Lloyd, T., . . . mechanobiology, m. i. (2020). The importance of blood rheology in patient-specific computational fluid dynamics simulation of stenotic carotid arteries. *19*(5), 1477-1490.
- Molina, M. C., Prause, G. P., Radeva, P., & Sonka, M. (1998). *3D catheter path reconstruction from biplane angiograms*. Paper presented at the Medical Imaging 1998: Image Processing.
- Morbiducci, U., Kok, A. M., Kwak, B. R., Stone, P. H., Steinman, D. A., Wentzel, J. J. J. T., & haemostasis. (2016). Atherosclerosis at arterial bifurcations: evidence for the role of haemodynamics and geometry. *115*(03), 484-492.
- Paritala, P. K., Yarlagadda, P. K. D. V., Wang, J., Gu, Y., & Li, Z. (2018). Numerical investigation of atherosclerotic plaque rupture using optical coherence tomography imaging and XFEM. *Engineering Fracture Mechanics*, *204*, 531-541. doi:<https://doi.org/10.1016/j.engfracmech.2018.11.002>
- Paritala, P. K., Yarlagadda, T., Mendieta, J. B., Wang, J., McGahan, T., Lloyd, T., . . . Li, Z. (2021). Plaque Longitudinal Heterogeneity in Morphology, Property, and Mechanobiology. *Cerebrovascular Diseases*, *50*(5), 510-519. doi:10.1159/000515690
- Ross, R. (1999). Atherosclerosis—an inflammatory disease. *New England journal of medicine*, *340*(2), 115-126.
- Saam, T., Ferguson, M., Yarnykh, V., Takaya, N., Xu, D., Polissar, N., . . . biology, v. (2005). Quantitative evaluation of carotid plaque composition by in vivo MRI. *25*(1), 234-239.
- Sforza, D. M., Putman, C. M., & Cebal, J. R. J. A. r. o. f. m. (2009). Hemodynamics of cerebral aneurysms. *41*, 91-107.
- Soldozy, S., Norat, P., Elsarrag, M., Chatrath, A., Costello, J. S., Sokolowski, J. D., . . . Park, M. S. J. N. f. (2019). The biophysical role of hemodynamics in the pathogenesis of cerebral aneurysm formation and rupture. *47*(1), E11.
- Steinman, D. A., Milner, J. S., Norley, C. J., Lownie, S. P., & Holdsworth, D. W. J. A. J. o. N. (2003). Image-based computational simulation of flow dynamics in a giant intracranial aneurysm. *24*(4), 559-566.
- Tang, D., Yang, C., Huang, S., Mani, V., Zheng, J., Woodard, P. K., . . . Fayad, Z. A. (2017). Cap inflammation leads to higher plaque cap strain and lower cap stress: An MRI-PET/CT-based FSI modeling approach. *J Biomech*, *50*, 121-129. doi:10.1016/j.jbiomech.2016.11.011
- Tang, D., Yang, C., Huang, S., Mani, V., Zheng, J., Woodard, P. K., . . . Fayad, Z. A. J. J. o. b. (2017). Cap inflammation leads to higher plaque cap strain and lower cap stress: an MRI-PET/CT-based FSI modeling approach. *50*, 121-129.
- Villablanca, J. P., Duckwiler, G. R., Jahan, R., Tateshima, S., Martin, N. A., Frazee, J., . . . Vinuela, F. V. J. R. (2013). Natural history of asymptomatic unruptured cerebral aneurysms evaluated at CT angiography: growth and rupture incidence and correlation with epidemiologic risk factors. *269*(1), 258-265.
- Virani, S. S., Alonso, A., Aparicio, H. J., Benjamin, E. J., Bittencourt, M. S., Callaway, C. W., . . . Delling, F. N. J. C. (2021). Heart disease and stroke statistics—2021 update: a report from the American Heart Association. *143*(8), e254-e743.
- Wang, J., Paritala, P. K., Mendieta, J. B., Komori, Y., Raffel, O. C., Gu, Y., . . . mechanobiology, m. i. (2020). Optical coherence tomography-based patient-specific coronary artery reconstruction and fluid–structure interaction simulation. *19*(1), 7-20.
- Williams, L. N., & Brown, R. D. J. N. C. P. (2013). Management of unruptured intracranial aneurysms. *3*(2), 99-108.
- Xu, P., Liu, X., Zhang, H., Ghista, D., Zhang, D., Shi, C., . . . mechanobiology, m. i. (2018). Assessment of boundary conditions for CFD simulation in human carotid artery. *17*(6), 1581-1597.
- Zhao, S., Xu, X., Hughes, A., Thom, S., Stanton, A., Ariff, B., & Long, Q. J. J. o. b. (2000). Blood flow and vessel mechanics in a physiologically realistic model of a human carotid arterial bifurcation. *33*(8), 975-984.